



JOURNAL OF
APPLIED
CRYSTALLOGRAPHY

Volume 56 (2023)

Supporting information for article:

Dynamic structural and microstructural responses of a metal-organic framework-type material to carbon dioxide under dual gas flow and supercritical conditions

Andrew J. Allen, Eric Cockayne, Winnie Wong-Ng, Jeffrey T. Culp and Ivan Kuzmenko

Supporting information

Dynamic structural and microstructural responses of a metal organic framework type material to carbon dioxide under dual gas flow and supercritical conditions

Authors

Andrew J. Allen^{a*}, Eric Cockayne^a, Winnie Wong-Ng^a, Jeffrey T. Culp^{bc} and Ivan Kuzmenko^d

^aMaterials Measurement Science Division, National Institute of Standards and Technology, 100 Bureau Drive, Gaithersburg, MD, 20899, USA

^bLRST/Battelle, NETL, Pittsburgh, PA, 15236, USA

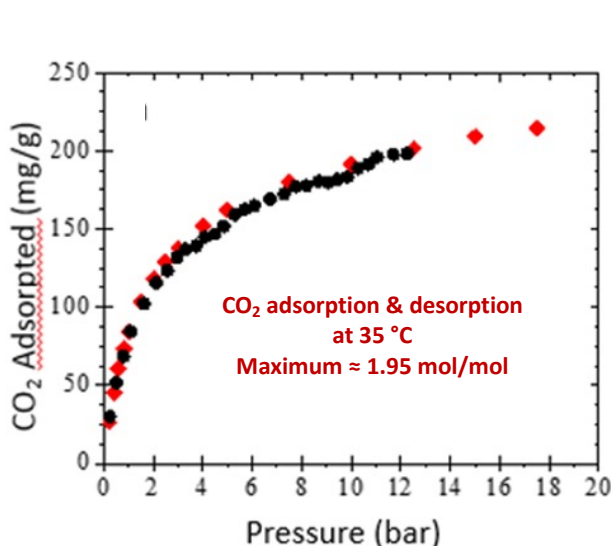
^cNational Energy Technology Laboratory, U.S. Department of Energy, Pittsburgh, PA, 15236, USA

^dX-ray Science Division, Argonne National Laboratory, 9700 South Cass Avenue, Argonne, IL, 60439, USA

Correspondence email: andrew.allen@nist.gov

ORCID NUMBERS: AJA: 0000-0002-6496-8411; EC: 0000-0002-4872-5946; WW: 0000-0002-6938-5936.

S1. CO₂ and other isotherms for Ni-BpyMe



(≈ 0.392 mol gas/mol Ni-BpyMe equates to 1 mmol/g, or CO₂: 44 mg/g; CH₄: 16 mg/g; N₂: 14 mg/g; H₂: 2 mg/g.)

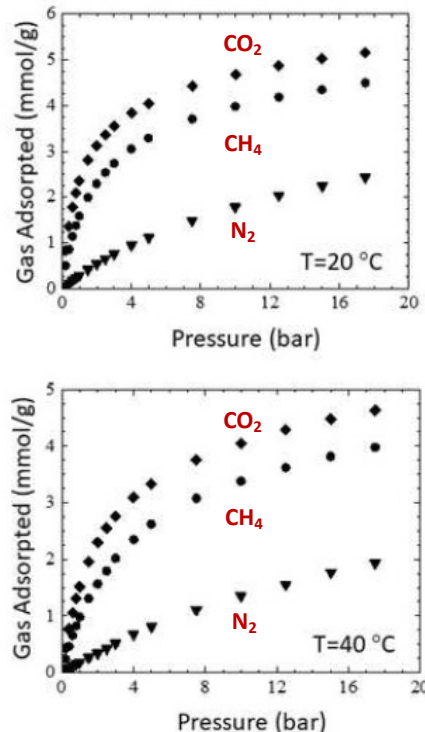


Figure S1. Adsorption/desorption CO₂ isotherms for Ni-BpyMe at 308 K (35 °C), and CO₂, CH₄, N₂ adsorption isotherms for Ni-BpyMe at 293 K (20 °C) and 313 K (40 °C). Measurement uncertainties are shown by data scatter but are generally smaller than the data points. (1 bar = 0.1 MPa)

Figure S1 presents previously published isotherms for Ni-BpyMe for CO₂, N₂ and CH₄ (Wong-Ng et al., 2016, 2021). These data show that Ni-BpyMe displays Type 1 isotherms for CO₂ sorption (also the case for N₂ and CH₄), that more gas is adsorbed at lower temperatures for comparable pressures, and that the molar uptake of CO₂ is greater than for CH₄, and much greater than for N₂.

S2. Typical USAXS/SAXS/WAXS data for Ni-BpyMe

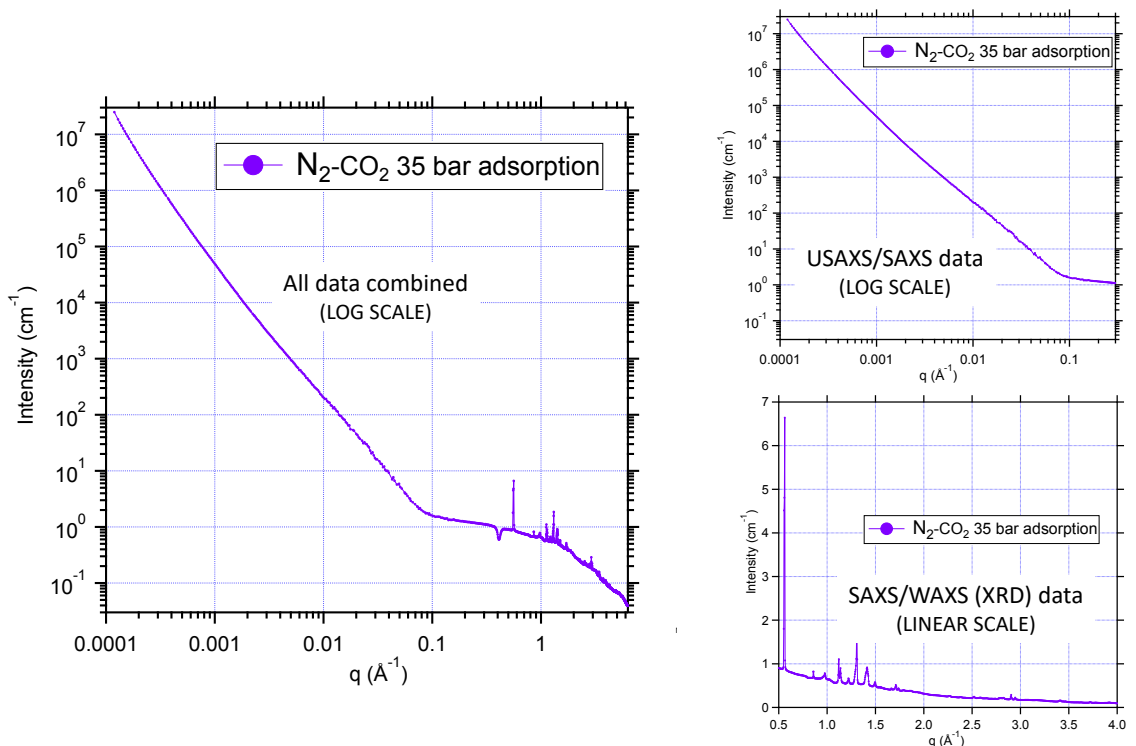


Figure S2. Typical combined slit-smeared USAXS data, sector-averaged pinhole SAXS data and sector-averaged WAXS data for Ni-BpyMe during CO₂/N₂ dual gas adsorption under a total pressure of 3.5 MPa (35 bar). Additional plots show combined USAXS/SAXS data for microstructural characterization, and combined SAXS/WAXS data for XRD analysis. Measurement uncertainties, generally comparable with data scatter, are omitted for clarity.

Figure S2 presents combined USAXS/SAXS/WAXS data over a contiguous q -range from 0.0001 Å⁻¹ to 6.3 Å⁻¹. Data were collected with appropriate Δ q / q resolution across the whole range in ≈ 6 min; – see Ilavsky et al., (2018). Combined USAXS/SAXS data are shown separately on a log-log plot in a q -range from 0.0001 Å⁻¹ to 0.3 Å⁻¹, before the flat background contribution is subtracted out. These data form the basis of the microstructural characterization discussed in this paper. Finally, combined SAXS/WAXS data in a q -range from 0.5 Å⁻¹ to 4.0 Å⁻¹ (small artifact at q ≈ 0.45 Å⁻¹ omitted and the sample pressure cell partially eclipses data for q > 4 Å⁻¹.) are shown on a linear-linear scale. The region of most interest for the XRD peaks studied here is 0.5 Å⁻¹ < q < 2 Å⁻¹. The intense XRD peak at ≈ 0.56 Å⁻¹ is the 001 peak, which does not move as gas is adsorbed or desorbed.

S3. Variations in USAXS/SAXS data during single or dual gas flow

During the subcritical single and dual gas flow studies using CO₂, N₂, CH₄ and H₂, changes in the measured scattering curve profiles remain subtle. The main observable change is an increase in intensity for $q > 0.1 \text{ \AA}^{-1}$ when more gas is present, either adsorbed by the matrix or at pressure in the void spaces. This is attributable to an increase in flat background and to an opening up and increased prominence of the nanoscale pores, as shown in **Figure 2a** in the main text. Combined slit-smeared USAXS/SAXS data profiles for the gas flow studies are presented here for information. In all cases the total gas flow rate is $\approx 100 \text{ mL/min}$. Total pressures are given in the legends. For dual gas flow the partial pressure for each gas is half the total pressure. Measurement uncertainties, represented by the small amount of data scatter, are omitted for clarity.

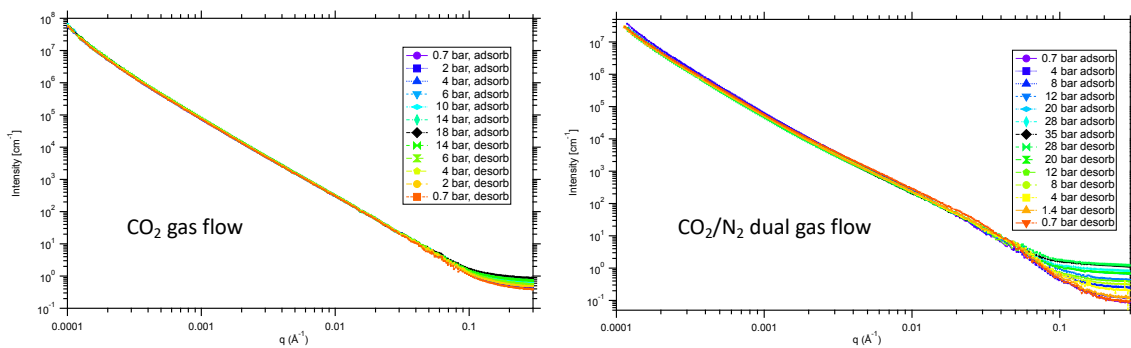


Figure S3. Slit-smeared USAXS/SAXS intensity data versus q for CO₂ and CO₂/N₂ gas flow.

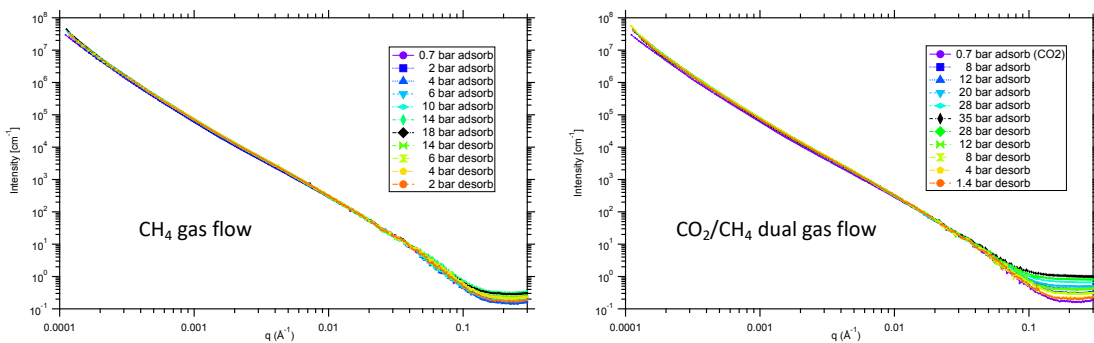


Figure S4. Slit-smeared USAXS/SAXS intensity data versus q for CH₄ and CO₂/CH₄ gas flow.

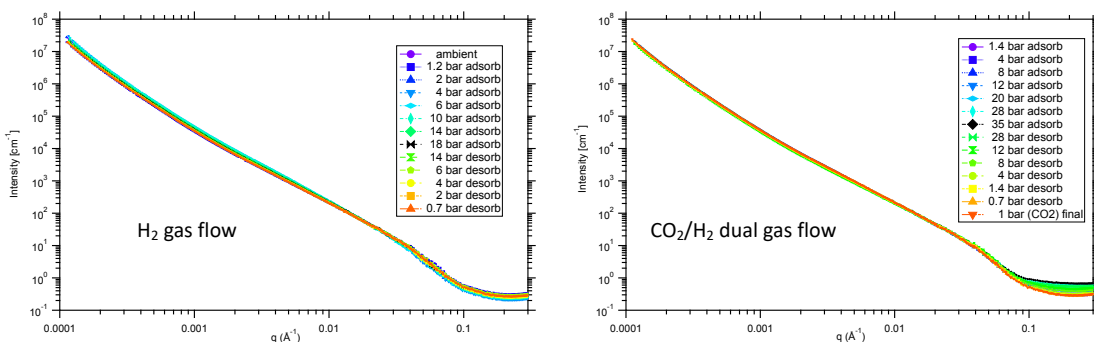


Figure S5. Slit-smeared USAXS/SAXS intensity data versus q for H₂ and CO₂/H₂ gas flow.

S4. Calculated changes in X-ray scattering contrast factor for CO₂ in Ni-BpyMe

Table S1 summarizes calculated fluid CO₂ and solid matrix Ni-BpyMe mass densities and X-ray scattering-length (form-factor) densities, ρ_X , and hence X-ray scattering contrast factors (squares of differences in ρ_X between CO₂ and matrix) for selected CO₂ adsorption conditions of interest.

Table S1 Calculated X-ray scattering contrast factors for CO₂ with Ni-BpyMe

| p (bar), T (°C) | CO ₂ density (g/cm ³) | CO ₂ state | CO ₂ ρ_X (10 ¹⁴ m ⁻²) | CO ₂ adsorbed (mmol/g) | Added CO ₂ to Ni-BpyMe density (g/cm ³) | Total ρ_X for solid Ni-BpyMe (10 ¹⁴ m ⁻²) | Contrast factor for CO ₂ with Ni-BpyMe (10 ²⁸ m ⁻⁴) |
|----------------------|---|-----------------------|---|---|--|--|---|
| 1, 90 | 0.00146 | GAS | 0.01230 | 0.000 | 0.00000 | 10.92108 | 119.00 |
| 5, 90 | 0.00738 | GAS | 0.06214 | 1.488 | 0.08033 | 11.59723 | 133.06 |
| 10, 90 | 0.01496 | GAS | 0.12593 | 2.425 | 0.13092 | 12.02301 | 141.54 |
| 20, 90 | 0.03075 | GAS | 0.25885 | 3.450 | 0.18626 | 12.48877 | 149.57 |
| 70, 90 | 0.12633 | GAS | 1.06329 | 3.450 | 0.18626 | 12.48877 | 130.54 |
| 74, 90 | 0.13553 | SC | 1.14072 | 3.500 | 0.18896 | 12.51149 | 129.29 |
| 78, 90 | 0.14502 | SC | 1.22057 | 3.500 | 0.18896 | 12.51149 | 127.48 |
| 78, 40 | 0.25716 | SC | 2.16443 | 4.750 | 0.25644 | 13.07950 | 119.14 |
| 78, 34 | 0.38374 | SC | 3.22983 | 4.800 | 0.25914 | 13.10222 | 97.46 |
| 78, 32 | 0.62420 | SC | 5.25376 | 4.850 | 0.26184 | 13.12494 | 61.96 |
| 78, 30 | 0.68866 | LIQ | 5.79627 | 5.000 | 0.26994 | 13.19310 | 54.71 |
| 74, 30 | 0.64744 | LIQ | 5.44936 | 5.000 | 0.26994 | 13.19310 | 59.97 |
| 72, 30 | 0.33199 | GAS | 2.79425 | 4.950 | 0.26724 | 13.17038 | 107.66 |
| 65, 30 | 0.20645 | GAS | 1.73764 | 4.950 | 0.26724 | 13.17038 | 130.71 |
| 65, 34 | 0.18882 | GAS | 1.58929 | 4.850 | 0.26184 | 13.12494 | 133.07 |
| 65, 40 | 0.17147 | GAS | 1.44320 | 4.700 | 0.25374 | 13.05678 | 134.88 |
| 70, 40 | 0.19803 | GAS | 1.66676 | 4.700 | 0.25374 | 13.05678 | 129.73 |
| 72, 40 | 0.21038 | GAS | 1.77074 | 4.700 | 0.25374 | 13.05678 | 127.37 |
| 74, 40 | 0.22408 | SC | 1.88602 | 4.750 | 0.25644 | 13.07950 | 125.29 |

| | | | | | | | |
|--------|---------|-----|---------|-------|---------|----------|--------|
| 78, 40 | 0.25716 | SC | 2.16443 | 4.750 | 0.25644 | 13.07950 | 119.14 |
| 78, 60 | 0.18388 | SC | 1.54767 | 4.250 | 0.22945 | 12.85230 | 127.79 |
| 74, 60 | 0.16921 | SC | 1.42423 | 4.250 | 0.22945 | 12.85230 | 130.60 |
| 70, 60 | 0.15554 | GAS | 1.30912 | 4.200 | 0.22675 | 12.82958 | 132.72 |
| 20, 60 | 0.03422 | GAS | 0.28801 | 4.200 | 0.22675 | 12.82958 | 157.29 |
| 10, 60 | 0.01646 | GAS | 0.13857 | 3.400 | 0.18356 | 12.46605 | 151.97 |
| 5, 60 | 0.00808 | GAS | 0.06804 | 2.575 | 0.13902 | 12.09117 | 144.56 |
| 1, 60 | 0.00159 | GAS | 0.01342 | 0.650 | 0.03509 | 11.21644 | 125.51 |

(SC = supercritical CO₂, LIQ = liquid CO₂; effect of thermal expansion on solid Ni-BpyMe density ignored)

Ni-BpyMe mass densities and CO₂ adsorption are derived from our previously published work (Wong-Ng et al., 2016 and 2021). CO₂ densities and phase information are derived from elsewhere (Span and Wagner, 1996). X-ray scattering lengths (X-ray form-factors at $q = 0$) are available from Chantler et al., 2005. In **Figure S6**, scattering contrast factors have been calculated for all conditions used in the supercritical CO₂ adsorption studies. The sequence segments followed in these studies are shown on the CO₂ phase diagram, together with the variations in scattering contrast factor between CO₂ and Ni-BpyMe matrix during each step, as explained in the main text.

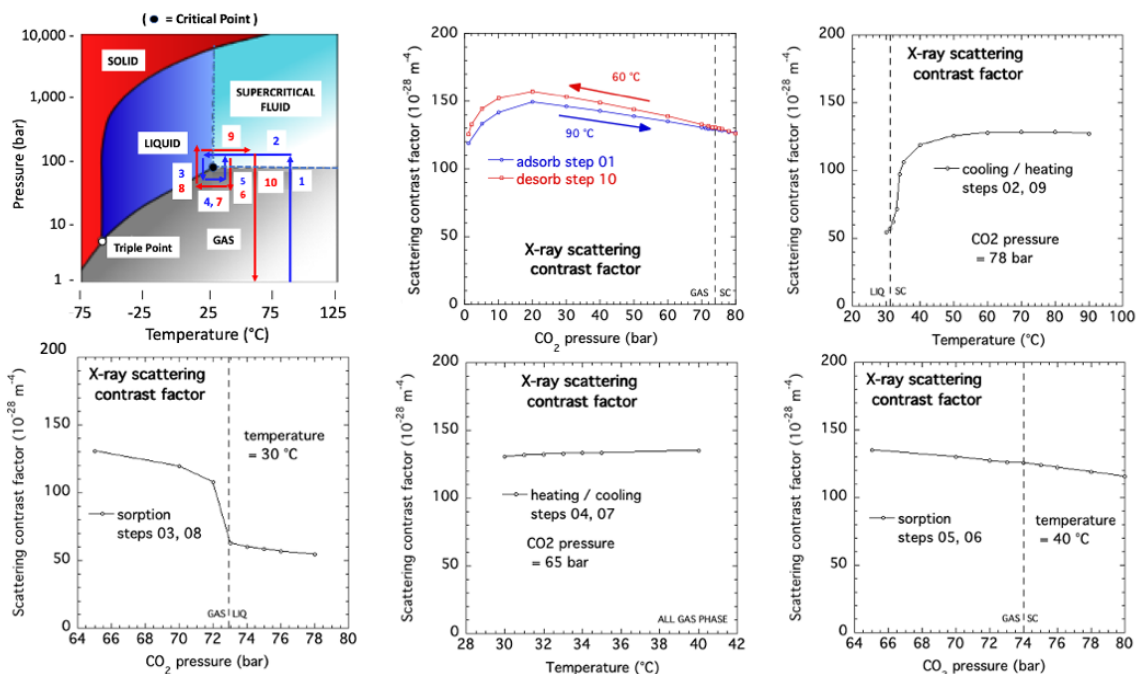


Figure S6. Trajectory followed in Ni-BpyMe supercritical CO₂ sorption studies around the CO₂ critical point, together with calculated X-ray scattering contrast factor variations for the various steps.

Clearly, the most striking aspect of the scattering contrast factor variation is its significant reduction when in the liquid CO₂ part (LIQ) of the phase diagram, or in the supercritical regime (SC) close to the liquid phase boundary. These data are important for interpreting changes in the associated USAXS/SAXS data profiles for each of the sequence steps discussed in the main text.

S5. Variations in USAXS/SAXS data during Ni-BpyMe supercritical CO₂ sorption studies

Combined slit-smeared USAXS/SAXS data profiles for the supercritical CO₂ sorption studies in Ni-BpyMe are presented here to supplement the discussion in the main text on the derived void size distributions, and how these change during each sequence step. Obvious changes in USAXS/SAXS profile are apparent, and not all are reversible. As for the gas flow studies, measurement uncertainties, represented by the small amount of data scatter, are omitted for clarity. We also present a full gallery of MaxEnt volume fraction size distributions, fine pore volume fractions and mean diameters, as well as coarse pore volume fractions and mean diameters. In these plots, vertical bars are estimated standard uncertainties based on similar measurements and analysis using the APS USAXS facility.

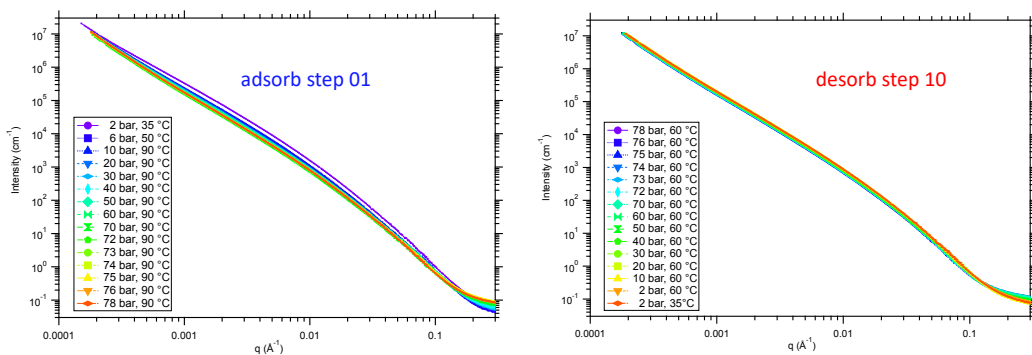


Figure S7. Slit-smeared USAXS/SAXS intensity data versus q for initial adsorption step at 363 K (90 °C) into the supercritical regime, and final desorption step from supercritical regime to ambient at 333 K (60 °C).

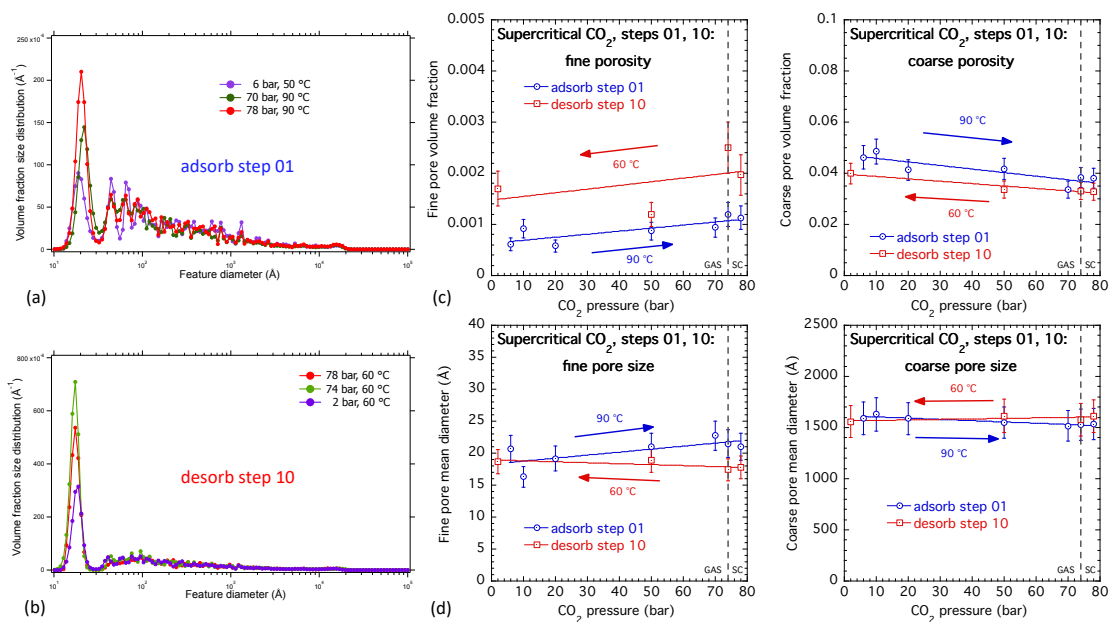


Figure S8. MaxEnt volume fraction size distribution for **(a)** step 1; **(b)** step 10; variations for steps 1 and 10 in **(c)** fine pore volume fraction; **(d)** fine pore mean diameter; **(e)** coarse pore volume fraction; **(f)** coarse pore mean diameter.

Apart from differences related to the different temperatures used, and some continuing activation of the sample in the initial adsorption step, the microstructural changes observed here on entry to or exit from the supercritical regime from/to the gas phase are largely reversible.

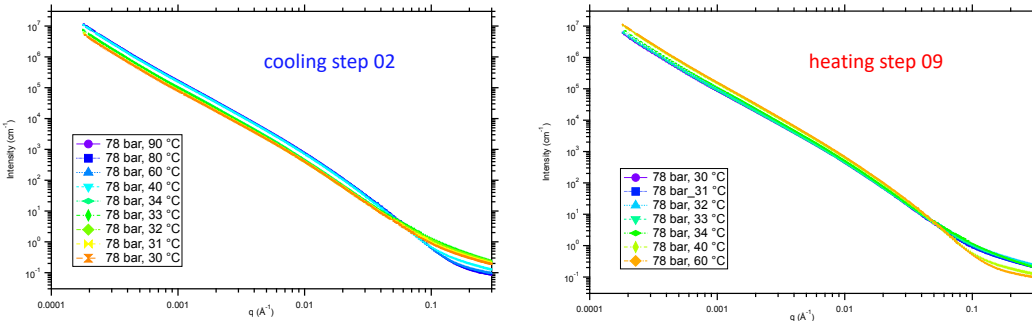


Figure S9. Slit-smeared USAXS/SAXS intensity data versus q for cooling/heating steps at 7.8 MPa (78 bar) CO_2 pressure from/to supercritical CO_2 phase to/from liquid CO_2 phase.

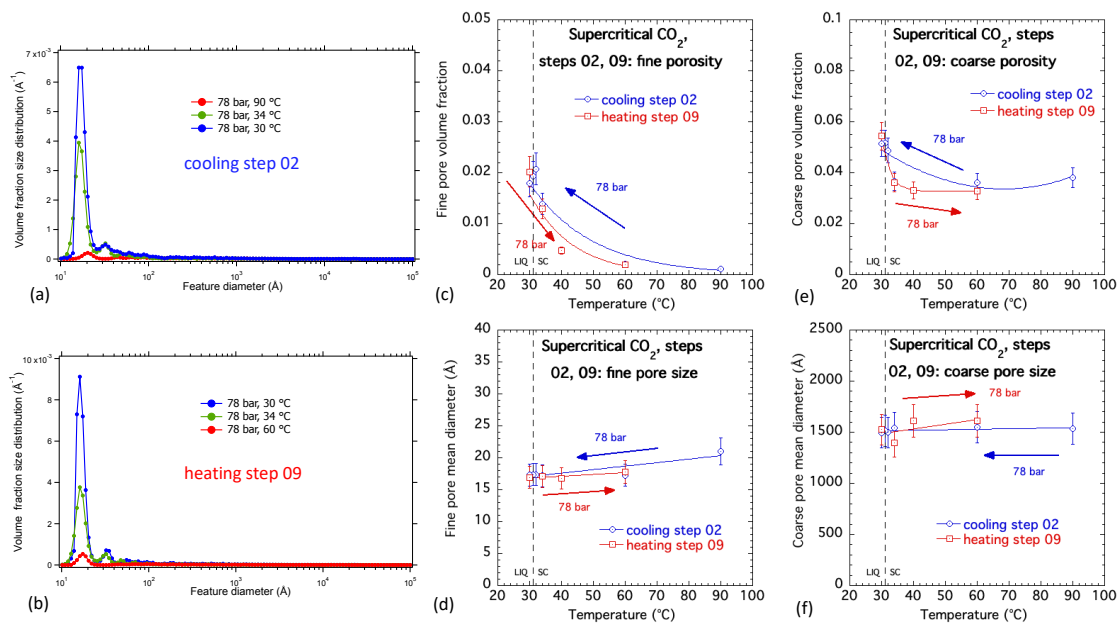


Figure S10. MaxEnt volume fraction size distribution for (a) step 2; (b) step 9; variations for steps 2 and 9 in (c) fine pore volume fraction; (d) fine pore mean diameter; (e) coarse pore volume fraction; (f) coarse pore mean diameter.

For the cooling and heating steps, 2 and 9, respectively, significant changes occur in the USAXS/SAXS profile, and hence in the microstructure, especially during the temperature-induced transitions to/from the liquid phase. While these changes reveal a very significant increase/decrease in the fine porosity, these changes remain largely reversible.

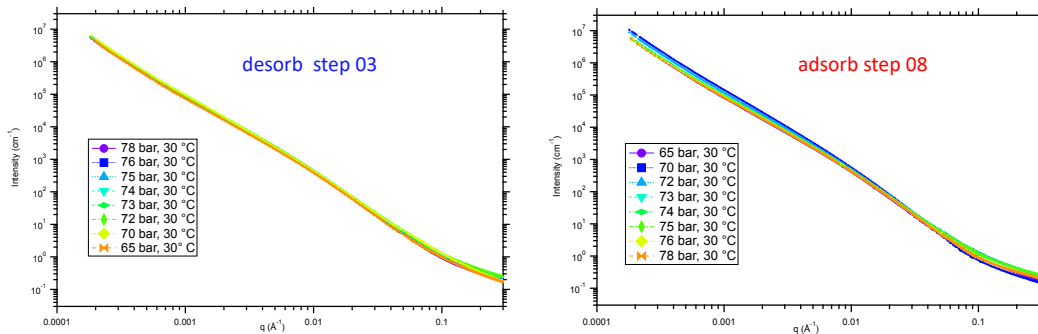


Figure S11. Slit-smeared USAXS/SAXS intensity data versus q for desorption and adsorption steps at 303 K (30 °C) from/to liquid phase to/gas phase.

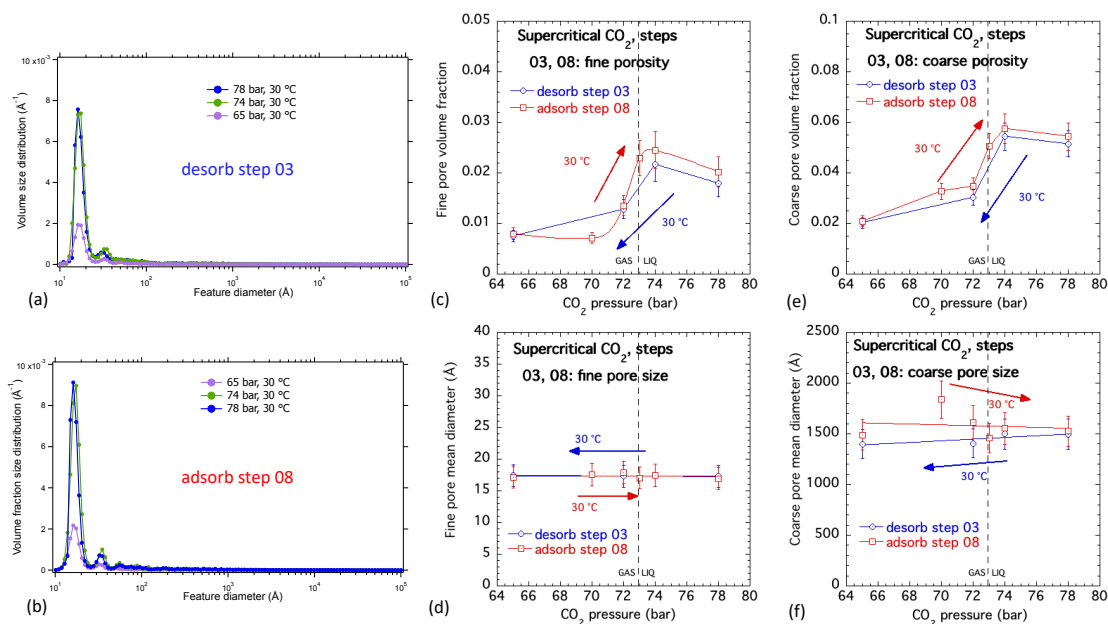


Figure S12. MaxEnt volume fraction size distribution for (a) step 3; (b) step 8; variations for steps 3 and 8 in (c) fine pore volume fraction; (d) fine pore mean diameter; (e) coarse pore volume fraction; (f) coarse pore mean diameter.

The changes associated with this pressure-mediated transition from/to liquid phase are not as fully reversible as steps 1 and 10 or steps 2 and 9. There are slightly more significant changes apparent for the pressure-induced transition from gas to liquid.

Although steps 4 and 7 occur wholly in the gas phase for CO_2 , some more significant but largely reversible changes are apparent especially in the relative proportions of fine and coarse pores at the lowest temperatures of the range:

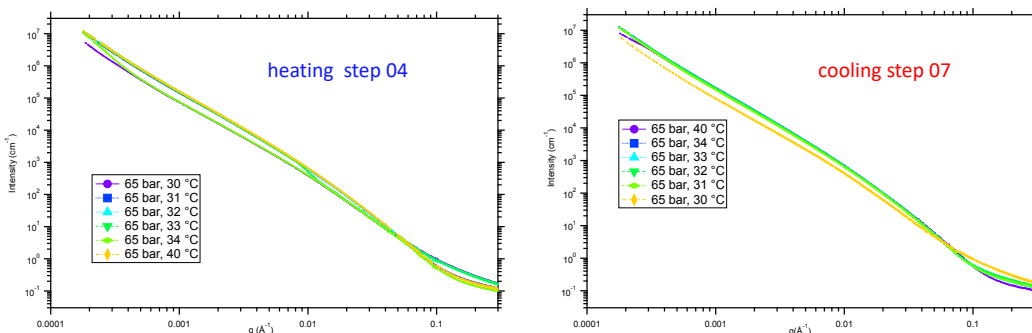


Figure S13. Slit-smeared USAXS/SAXS data versus q for heating and cooling steps at 6.5 MPa (65 bar) CO_2 pressure.

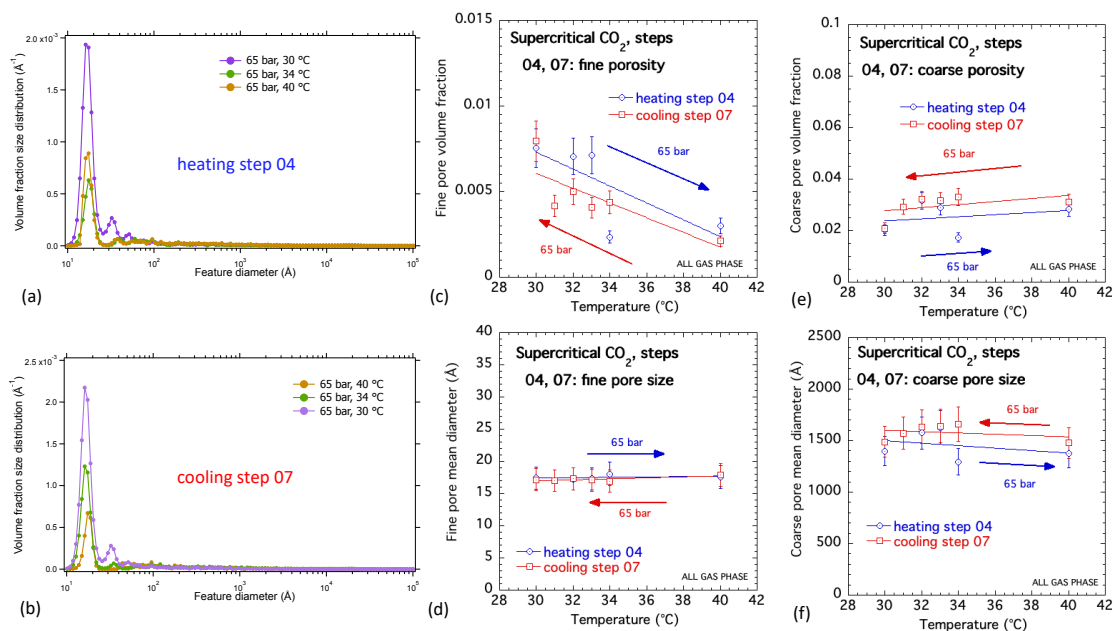


Figure S14. MaxEnt volume fraction size distribution for (a) step 4; (b) step 7; variations for steps 4 and 7 in (c) fine pore volume fraction; (d) fine pore mean diameter; (e) coarse pore volume fraction; (f) coarse pore mean diameter.

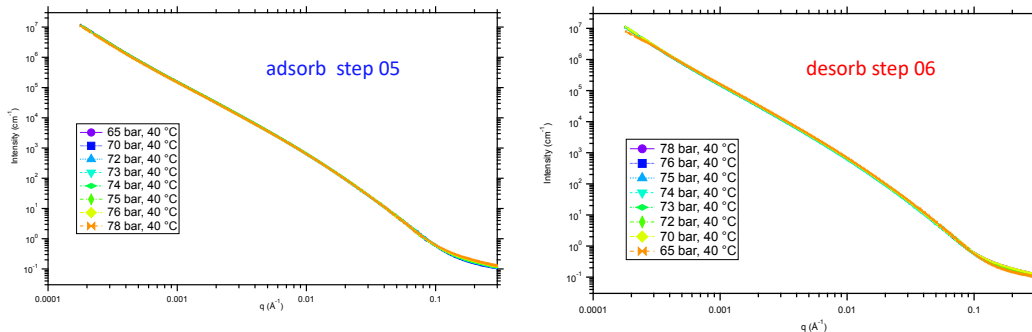


Figure S15. Slit-smeared USAXS/SAXS data versus q for adsorption and desorption steps at 313 K (40 °C) from/to gas phase to/from supercritical phase. Only subtle reversible changes are observed.

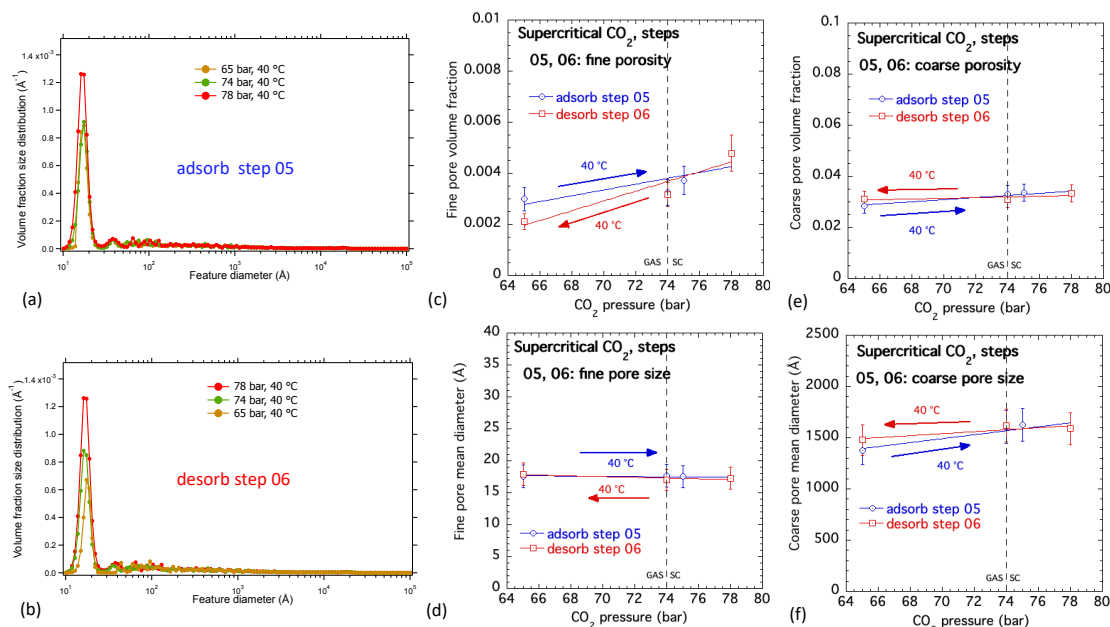


Figure S16. MaxEnt volume fraction size distribution for (a) step 5; (b) step 6; variations for steps 5 and 6 in (c) fine pore volume fraction; (d) fine pore mean diameter; (e) coarse pore volume fraction; (f) coarse pore mean diameter.

While some significant changes in the USAXS/SAXS profile during the measurement sequence are observed, most changes in the curves and associated microstructure are reversible. The most significant irreversible step-changes are associated with pressure-induced transitions between the liquid and gas CO_2 regimes.

References (also referenced in main paper)

- Chantler, C.T., Olsen, K., Dragoset, R.A., Chang, J., Kishore, A.R. Kotchigova, S.A. & Zucker, D.S. (2005). *X-ray Form Factor, Attenuation, and Scattering Tables* (Version 2.1). NIST, Gaithersburg, Maryland, USA, <http://physics.nist.gov/ffast>.
- Ilavsky, J., Zhang, F., Andrews, R.N., Kuzmenko, I., Jemian, P.R., Levine, L.E. & Allen, A.J. (2018). *J. Appl. Cryst.*, **51**, 867-882. DOI:10.1107/S160057671800643X
- Span, R. & Wagner, W. (1996). *J. Phys. Chem. Ref. Data*, **25**, 1509-1596. DOI:10.1063/1.555991
- Wong-Ng, W., Culp, J. & Chen, Y.-S. (2016). *Crystals*, **6**, art.108. DOI:10.3390/crust6090108
- Wong-Ng, W., Culp, J., Siderius, D.W., Chen, Y., Wang, S.Y.G., Allen A.J. & Cockayne, E. (2021). *Polyhedron*, **200**, art. 115132. DOI:10.1016/j.poly.2021.115132